

PAPER • OPEN ACCESS

Linking topological features of the Hofstadter model to optical diffraction figures

To cite this article: Francesco Di Colandrea *et al* 2022 *New J. Phys.* **24** 013028

View the [article online](#) for updates and enhancements.

You may also like

- [A study of the ambiguity in the solutions to the Diophantine equation for Chern numbers](#)
J E Avron, O Kenneth and G Yehoshua
- [Parametric instabilities in resonantly-driven Bose–Einstein condensates](#)
S Lellouch and N Goldman
- [Hofstadter's butterfly in quantum geometry](#)
Yasuyuki Hatsuda, Hosho Katsura and Yuji Tachikawa











OPEN ACCESS

RECEIVED
25 June 2021REVISED
3 December 2021ACCEPTED FOR PUBLICATION
8 December 2021PUBLISHED
19 January 2022Original content from
this work may be used
under the terms of the
[Creative Commons
Attribution 4.0 licence](#).Any further distribution
of this work must
maintain attribution to
the author(s) and the
title of the work, journal
citation and DOI.

PAPER

Linking topological features of the Hofstadter model to optical diffraction figures

Francesco Di Colandrea^{1,8} , Alessio D'Errico^{1,8} , Maria Maffei², Hannah M Price³ ,
Maciej Lewenstein^{4,5} , Lorenzo Marrucci^{1,6} , Filippo Cardano^{1,*} ,
Alexandre Dauphin^{4,*}  and Pietro Massignan^{4,7} ¹ Dipartimento di Fisica, Università di Napoli Federico II, Complesso Universitario di Monte Sant'Angelo, Via Cintia, 80126 Napoli, Italy² Université Grenoble Alpes, CNRS, Grenoble INP, Institut Néel, 38000 Grenoble, France³ School of Physics and Astronomy, University of Birmingham, Edgbaston, Birmingham B15 2TT, United Kingdom⁴ ICFO—Institut de Ciències Fotòniques, The Barcelona Institute of Science and Technology, 08860 Castelldefels (Barcelona), Spain⁵ ICREA, Pg. Lluís Companys 23, 08010 Barcelona, Spain⁶ CNR-ISASI, Institute of Applied Science and Intelligent Systems, Via Campi Flegrei 34, 80078 Pozzuoli (NA), Italy⁷ Departament de Física, Universitat Politècnica de Catalunya, Campus Nord B4-B5, 08034 Barcelona, Spain

* Authors to whom any correspondence should be addressed.

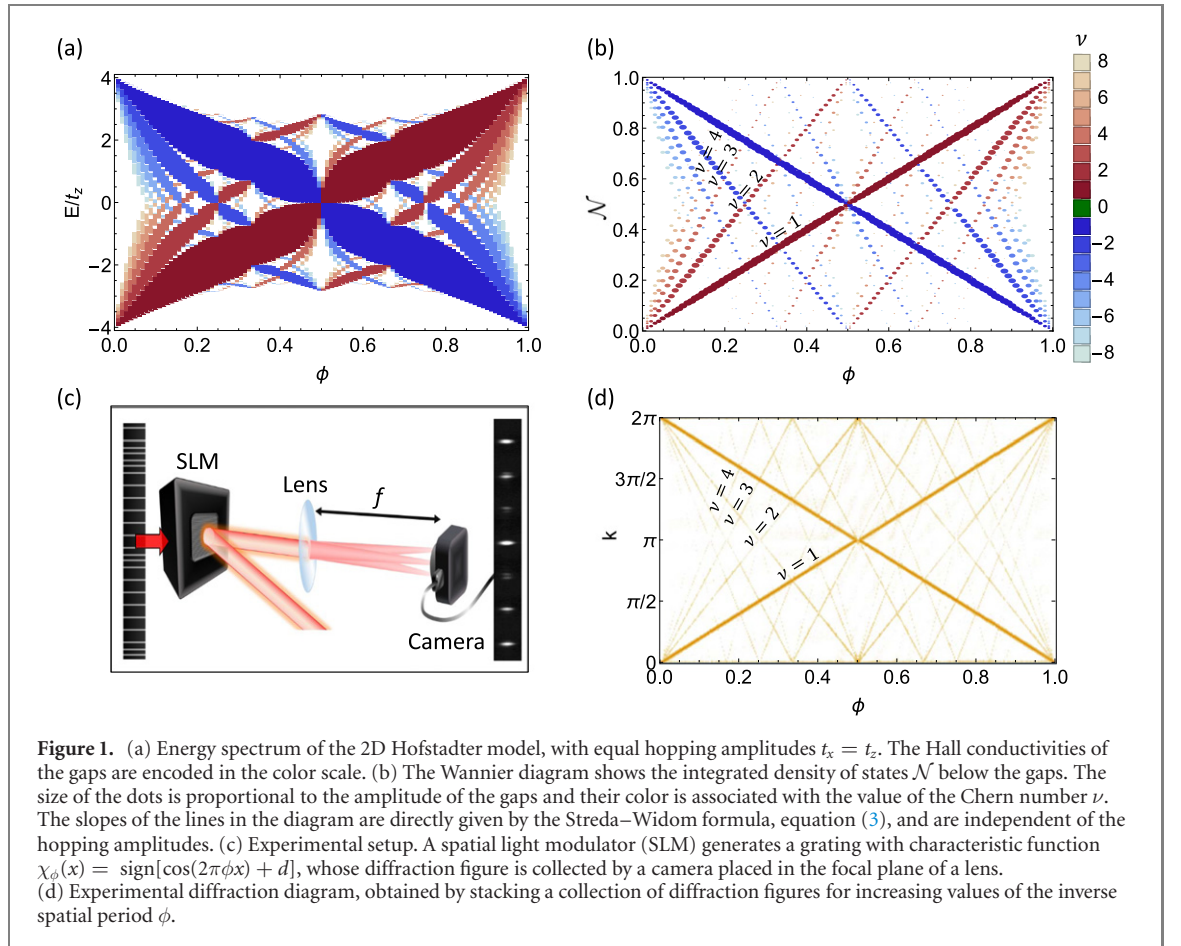
⁸ These two authors contributed equally.E-mail: filippo.cardano2@unina.it and Alexandre.dauphin@icfo.eu**Keywords:** topological physics, Hofstadter model, quantum Hall effect, optics

Abstract

In two, three and even four spatial dimensions, the transverse responses experienced by a charged particle on a lattice in a uniform magnetic field are fully controlled by topological invariants called Chern numbers, which characterize the energy bands of the underlying Hofstadter Hamiltonian. These remarkable features, solely arising from the magnetic translational symmetry, are captured by Diophantine equations which relate the fraction of occupied states, the magnetic flux and the Chern numbers of the system bands. Here we investigate the close analogy between the topological properties of Hofstadter Hamiltonians and the diffraction figures resulting from optical gratings. In particular, we show that there is a one-to-one relation between the above mentioned Diophantine equation and the Bragg condition determining the far-field positions of the optical diffraction peaks. As an interesting consequence of this mapping, we discuss how the robustness of diffraction figures to structural disorder in the grating is a direct analogue of the robustness of transverse conductance in the quantum Hall effect.

Exposing an electronic crystal to a magnetic field radically alters its physical properties. A celebrated example is the integer quantum Hall effect (IQHE), where a perpendicular magnetic field converts a two-dimensional (2D) metal into a Chern insulator [1]. This physics is captured by the fractal spectrum (or 'butterfly') of the Hofstadter model [2], which features smooth bands characterized by integer topological invariants named Chern numbers. The transverse conductance in each energy gap, depicted in figure 1(a), is given by the sum of the Chern numbers of the occupied bands [3, 4], which ensures their robustness against local perturbations, such as interactions or disorder [5]. The physics becomes notably richer in higher spatial dimensions. A 3D metal exposed to a magnetic field was shown to exhibit quantized transverse conductivities in various 2D planes, determined by a triad of total first Chern numbers [6–17]. In 4D, the response of the system to an external electro-magnetic field is governed by a more complex invariant called second Chern number [18–32].

Currently, very strong *synthetic* magnetic fields can be engineered in a variety of quantum simulators [33–35], allowing for the observation of the 2D and 4D IQHE in various atomic [27, 36, 37], photonic [28, 38–40] and acoustic [31, 41] platforms. On the other hand, the 3D case was recently observed in a solid-state ZrTe₅ crystal [42]. In general, traditional transport measurements in artificial platforms proved



feasible [43], but not straightforward. As such, strong efforts are presently being undertaken to develop new methods for the characterization of the underlying topology [37, 38, 44–49].

In this work, we show that the topological features of the 2D, 3D and 4D IQHE can be linked to the properties of optical diffraction figures. Indeed, the peculiar translational symmetry of the Hofstadter Hamiltonian can be encoded in periodic phase gratings (diffraction gratings) dynamically generated by a spatial light modulator (SLM), and the magnetic flux piercing the lattice may be controlled by adjusting their spatial period. As we will show, the diffraction pattern produced by the grating bears close analogies to the *Wannier diagram* resulting from the Hofstadter model [50], and the slopes of the various lines directly yield the Chern numbers of the corresponding spectral gaps.

1. Lorentz vs density responses

The Chern numbers of the 2D IQHE can be measured through the response of a system to (synthetic) electromagnetic fields.

One class of such experiments measures the *Lorentz-type* response to a weak force. This is realized, for example, by preparing a localized wavefunction and reading out the displacement of its center-of-mass along the direction perpendicular to the force [25, 36, 40, 51, 52], or by applying dimensional reduction to obtain an effective 1D time-periodic model and observing the consequent quantized displacement across the bulk of the system (‘Thouless pumping’) [53–55]. The latter approach has also been adopted for irrational values of the flux ϕ , which give rise, through dimensional reduction, to 1D quasi-crystals [56], i.e. crystalline structures which are not periodic, but nonetheless exhibit long-range order [38, 57–60]. In particular, the Chern number of a 1D quasi-crystal has been measured in a diffraction experiment through a Lorentz-type measurement in reference [58].

In a second line of experiments, which is the one we follow here, one instead probes a *density-type* response by gradually changing the magnetic flux piercing the lattice. As first discussed by Wannier in reference [50], even a small change in the flux radically modifies the underlying band structure, thereby altering the integrated density of states (i.e. the fraction of occupied bands). This may be conveniently displayed in a so-called *Wannier diagram*, which shows how the density of states grows linearly with the

magnetic flux. Subsequent works [61–63] proved that the linear coefficient which links the density of states and the magnetic flux is proportional to the Hall conductivity. In particular, these studies highlighted that the complete topological information about the 2D Hofstadter model is fully encoded in its Wannier diagram [63]. As we will show in the following, this applies also to its generalizations to three [8, 9] and four [23–25] dimensions.

2. 2D Hofstadter model

Let us consider spinless fermions on a square lattice in the xz plane, subject to a magnetic flux $\phi = p/q$ per plaquette, with integers p and q (we set $e = \hbar = a = 1$, where a is the lattice spacing). In the Landau gauge with periodic boundary conditions in the z -direction, the eigenvalue problem reduces to the Harper equation [64], which reads

$$[E_{n\mathbf{k}} + 2t_z \cos(2\pi\phi x + k_z)] u_{n\mathbf{k}}(x) = -t_x [e^{ik_x} u_{n\mathbf{k}}(x+1) + e^{-ik_x} u_{n\mathbf{k}}(x-1)], \quad (1)$$

where $u_{n\mathbf{k}}(x)$ is the Bloch function for the n th band, with quasi-momentum \mathbf{k} in the reduced Brillouin zone (RBZ): $k_x \in [0, 2\pi/q]$ and $k_z \in [0, 2\pi]$.

The energy spectrum as a function of the magnetic flux ϕ , shown in figure 1(a), is the famous Hofstadter butterfly, which displays an intriguing fractal structure. At zero temperature, the Hall conductivity σ_r^{xz} in the r th energy gap equals the sum of the Chern numbers of the r occupied bands [3]

$$\nu = \sum_{n \leq r} \int_{\text{RBZ}} \Omega_n^{xz} d^2k / 2\pi, \quad (2)$$

defined in terms of the Berry curvature of the n th band $\Omega_n^{xz} = i [\langle \partial_{k_x} u_{n\mathbf{k}} | \partial_{k_z} u_{n\mathbf{k}} \rangle - \langle \partial_{k_z} u_{n\mathbf{k}} | \partial_{k_x} u_{n\mathbf{k}} \rangle]$. Alternatively, the Hall conductivity can also be derived from the Streda–Widom formula $\nu = \partial_\phi \mathcal{N}$ [61], where $\mathcal{N} \equiv r/q$ denotes the integrated density of states below the r th energy gap. This formula is very general, and holds true also for incompressible fractional Chern insulator phases [65], where the Hall conductivity is directly proportional to the many-body Chern number. For the 2D Hofstadter model, the Streda–Widom formula leads to the celebrated Diophantine equation

$$r/q = \phi\nu + s, \quad (3)$$

which has a unique integer solution ν for a set of integers p, q, r, s , assuming p and q are coprime, $0 < r < q$ and $|\nu| < q/2$. As shown by Dana *et al* [63], the Diophantine equation can also be derived from the properties of the magnetic translation operators. Their elegant proof, which we review in appendix C, only requires the periodicity of the wavefunction. The Diophantine equation can also be derived with the help of perturbation theory in the weak-coupling limit $t_x \ll t_z$ [4]. Remarkably, within this limit one can show that both the transverse conductivity and the quasi-momenta at which energy gaps open follow the *same Diophantine equation*.

Here, we take advantage of the relation between the Bragg condition and the Diophantine equation to recover the Hofstadter butterfly through a 1D diffraction experiment. In fact, by exhibiting the same spatial periodic structure as the Harper onsite (cosine) potential, Bragg diffraction proves to be an ideal candidate to study key topological features of the Hofstadter model. The Lorentz-type measurement of reference [58] required direct access to the complex phase of the diffracted wave, which was ingeniously extracted through an interferometric scheme. Here we discuss a conceptually different and much simpler density-type experiment, which only requires measuring the far-field intensity of light. A detailed description of our optical setup can be found in appendix A.

In a first experiment, we write on an SLM a 1D diffraction grating generated by the characteristic function

$$\chi_\phi(x) = \text{sign}[\cos(2\pi\phi x) + d], \quad (4)$$

which generates a periodic figure with spatial period $1/\phi$. The choice of the non-linear ‘sign’ function is mainly dictated by a practical convenience, as it enables one to observe many harmonics, thus allowing for a more accurate reconstruction of the diffraction diagram. Furthermore, it can be displayed on the SLM with high fidelity and exploiting the full resolution of the device. In principle, however, any other grating preserving the spatial periodicity of the original magnetic unit cell could be adopted. The diffraction figure collected out of this structure contains a series of sharp Bragg peaks, as shown in figure 1(c). The relative intensity of the peaks can be controlled by tuning the dimensionless constant d . We set $d = 0.25$ to ensure the best visibility of the main orders of diffraction. The position of the peaks can be derived from the

Fourier transform of the grating (explicitly computed in appendix B), and is simply given by the *Bragg condition*

$$k/(2\pi) = \phi\nu + s, \quad (5)$$

with ν and s integer numbers, and $k/2\pi = l/L$ is the ratio between an integer l and the lattice size L . The latter condition requires that diffraction peaks are spaced by integer multiples of the RBZ. The Bragg condition is therefore a direct analogue of the Diophantine equation (3). Figure 1(d) depicts the *diffraction diagram*, obtained by arranging side-by-side the diffraction figures generated by the grating for increasing values of ϕ . The slopes of the lines forming the diagram correspond to the values of ν , and the diffraction diagram is in a 1-to-1 correspondence with the Wannier diagram obtained from the density of states shown in figure 1(b). We point out that we are probing the topology of the bands which emerges from the traditional derivation, i.e. by means of the *Peierls substitution* [4]. Our approach would also apply to the Hofstadter butterfly spectrum resulting from the exact (numerical) calculation, since the topological Wannier diagram is preserved [66].

We have also investigated the effects of structural disorder or different characteristic functions χ on the diffraction diagram, and found that its main features are robust, as expected for topological properties. This will be presented in detail in section 5.

3. 3D Hofstadter model

The Hofstadter model is generalized to three spatial dimensions by considering a magnetic field having components along the three vectors spanning the cubic lattice [8, 9, 13–15]. Here we consider the particular case of a magnetic field $\mathbf{B} = (0, \phi_y, \phi_z)$, where $\phi_y = p_y/q_y$ ($\phi_z = p_z/q_z$) is the magnetic flux through the $xz(xy)$ plane. In the 3D analogue of the Landau gauge, the Harper equation reads

$$[E_{nk} + 2t_y \cos(2\pi\phi_z x + k_y) + 2t_z \cos(2\pi\phi_y x - k_z)] u_{nk}(x) = -t_x [e^{ik_x} u_{nk}(x+1) + e^{-ik_x} u_{nk}(x-1)]. \quad (6)$$

This eigenvalue problem has Q solutions, Q being the least common multiple of q_y and q_z , and the RBZ is defined by $0 < k_x \leq 2\pi/Q$, $0 < k_y, k_z \leq 2\pi$. The separation among the Q energy bands depends on the relative amplitudes of the hopping, and in the limit $t_x \gg t_y, t_z$ the system exhibits the maximum number of $Q - 1$ gaps [8]. These gaps are characterized by a triad of first Chern numbers (ν_x, ν_y, ν_z) . These invariants appear in the quantization of the transverse conductivity in the planes defined by the unit vector of the cubic lattice. In our case, one finds $\sigma^{xy} = \nu_z$, $\sigma^{xz} = -\nu_y$ and $\sigma^{yz} = \nu_x = 0$. The integrated density of states is related to the rational fluxes by a 3D version of the Diophantine equation [8, 9]:

$$\mathcal{N} \equiv r/Q = \phi_y \nu_y + \phi_z \nu_z + s, \quad (7)$$

where s and ν_α ($\alpha = \{y, z\}$) are integers. As in the 2D case, this relation arises directly from the magnetic translational symmetry of the system (see appendix D). The 3D Diophantine equation admits a unique solution for every set r, p_y, p_z, q_y, q_z , for q_y and q_z coprime integers, $0 < r < Q$, $|\nu_y| < q_y/2$ and $|\nu_z| < q_z/2$. The transverse conductivity in the different planes can therefore be computed with the help of the generalized Streda–Widom formula $\sigma_{ij} = \epsilon_{ijk} \partial_{\phi_k} \mathcal{N}$.

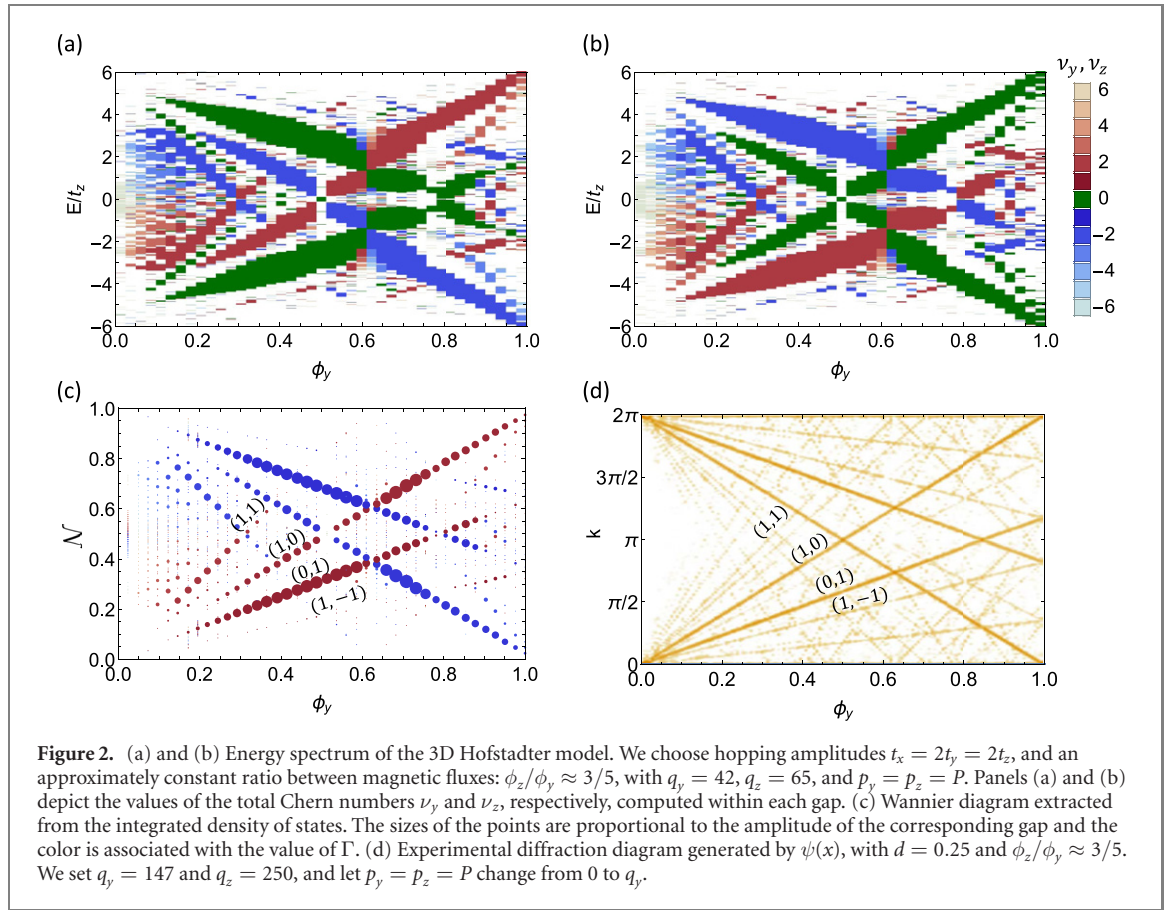
We now study the Hofstadter butterfly and the Wannier diagram resulting from the 3D quantum Hall lattice. There are many ways one can change the magnetic field, for example: (i) changing its orientation with respect to the unit cell while keeping its amplitude fixed [13], (ii) changing its amplitude while keeping its orientation fixed [8, 14]. Here we adopt the second strategy, choosing the magnetic fluxes as $\phi_y = m_y P/Q$ and $\phi_z = m_z P/Q$. The Diophantine equation (7) then reads

$$\mathcal{N} = s + \Gamma P/Q, \quad (8)$$

where we have introduced a ‘combined’ first Chern number $\Gamma = \nu_y m_y + \nu_z m_z$. Figures 2(a) and (b) show the Hofstadter butterfly generated for $t_x = 2t_y = 2t_z$ and a constant ratio between the fluxes $\phi_z/\phi_y \approx 3/5$. In the two panels, the color of the gaps corresponds to the values of ν_y and ν_z , respectively. Figure 2(c) shows the Wannier diagram of the 3D Hofstadter model derived from the integrated density of states (here the colors of the points correspond to the values of Γ). As an optical topological probe, we arranged a second experiment where we write on the SLM a 1D diffraction grating generated by the characteristic function

$$\psi(x) = \text{sign}[\cos(2\pi\phi_y x) + \cos(2\pi\phi_z x) + d]. \quad (9)$$

As in the 2D case, we set the constant $d = 0.25$ to improve the visibility of the main diffraction orders. The peaks are centered at $k = 2\pi [\phi_y \nu_y + \phi_z \nu_z + s]$. Again, the translational symmetry of $\psi(x)$ ensures that the



position of the Bragg peaks obeys the Diophantine equation (7). We reconstruct the Wannier diffraction diagram by arranging side-by-side the diffraction figures generated by the grating for different values of ϕ_y . The slopes of the lines forming the diagram correspond to the values of Γ (see figure 2(d)). Also for the 3D case, we found an excellent agreement between the diffraction diagram and the Wannier diagram (see figure 2(c)).

4. 4D Hofstadter model

4.1. 4D decoupled Hofstadter model

The simplest model exhibiting the 4D IQHE is obtained by superposing two copies of the Hofstadter model, with a magnetic tensor having two non-zero components $B_{xz} = \phi_x$ and $B_{yw} = \phi_y$ [23, 25, 57]. The corresponding Hamiltonian leads to the following Harper equation:

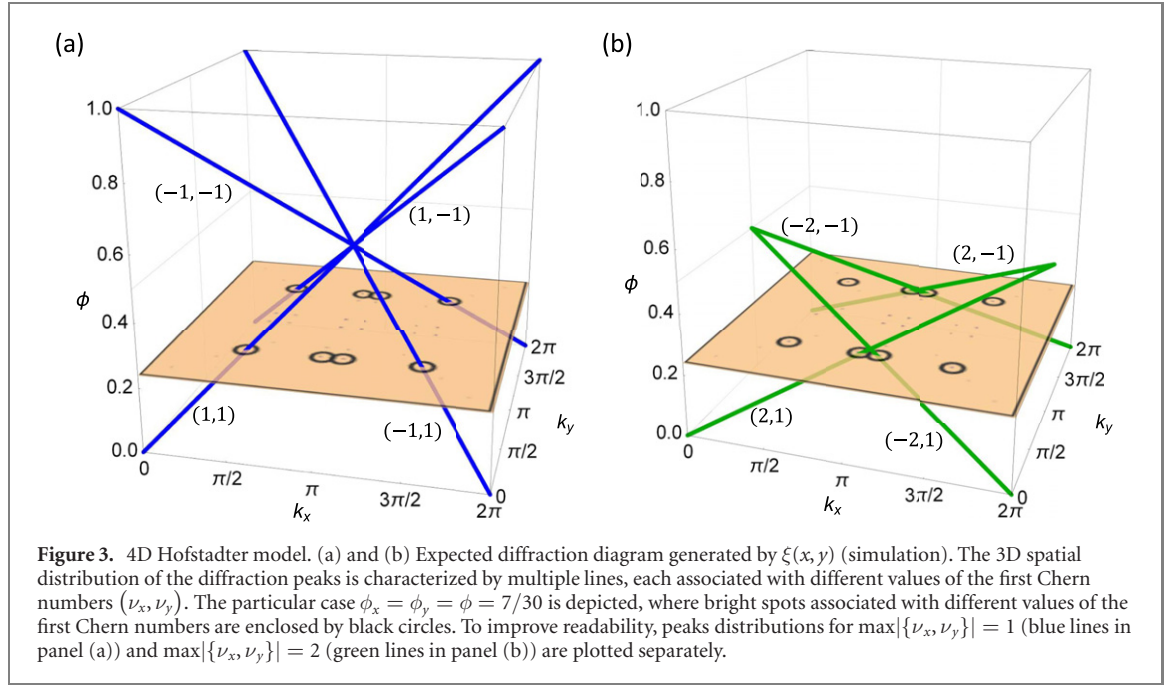
$$\begin{aligned}
 E_{\mathbf{n}\mathbf{k}} u_{\mathbf{n}\mathbf{k}}(x, y) = & - \left[2t_z \cos(2\pi\phi_x x + k_z) + 2t_w \cos(2\pi\phi_y y + k_w) \right] u_{\mathbf{n}\mathbf{k}}(x, y) \\
 & - t_x \left[e^{ik_x} u_{\mathbf{n}\mathbf{k}}(x+1, y) + e^{-ik_x} u_{\mathbf{n}\mathbf{k}}(x-1, y) \right] \\
 & - t_y \left[e^{ik_y} u_{\mathbf{n}\mathbf{k}}(x, y+1) + e^{-ik_y} u_{\mathbf{n}\mathbf{k}}(x, y-1) \right].
 \end{aligned} \tag{10}$$

In this ‘minimal’ 4D model, as the planes having non-zero Berry curvatures are fully decoupled, the second Chern number C_2 is simply the product of the two first Chern numbers ν_x and ν_y . We will show that our approach also applies in the case in which the planes are coupled and the second Chern number is not factorizable.

After invoking the two commuting magnetic translation symmetries of the system along x and y , one is led to two independent Diophantine equations, which may be multiplied to obtain

$$\mathcal{A} = (\nu_x \phi_x + s_x)(\nu_y \phi_y + s_y), \tag{11}$$

where \mathcal{A} is the fraction of filled bands in the system at zero temperature. As familiar from the *Gedanken-experiment* proposed by Laughlin [67], changing the magnetic flux across the system effectively induces a ‘density-response’ which alters the band-filling in a way that is proportional to the Chern



numbers. In particular, the first total Chern numbers ν_x and ν_y are given by $\nu_\alpha = (1/s_\beta)\partial_{\phi_\alpha}\mathcal{A}|_{\phi_\beta=0}$, and the second total Chern number is $C_2 = \partial_{\phi_x}\partial_{\phi_y}\mathcal{A} = \nu_x\nu_y$. In a third experimental realization, we would suggest to write on the SLM a 2D diffraction grating generated by the characteristic function

$$\xi(x, y) = \text{sign}[\cos(2\pi\phi x) + \cos(2\pi\phi y) + d], \quad (12)$$

where we set $\phi_x = \phi_y = \phi$. The diffraction pattern generated by the grating defined above exhibits a series of bright spots placed at $\mathbf{k} = 2\pi\{(\phi\nu_x + s_x), (\phi\nu_y + s_y)\}$ (see figure 3). As in the previous experiments, a constant offset d may be added to reinforce the visibility of the main spectral gaps. After stacking the 2D diffraction figures generated for different values of ϕ in a 3D plot, a Wannier diffraction diagram is obtained, where the coordinates of the points are given by two Diophantine equations, and the area under each line is given by equation (11) (see figure 3). We finally emphasise that this setup also allows one to reproduce diffraction figures featuring the same topology (in the sense discussed in section 2) as a class of 2D quasi-crystals, corresponding to the dimensional reduction of the 4D quantum Hall effect with irrational fluxes [23, 27, 28].

4.2. 4D coupled Hofstadter model

Until now we focused on the simplest version of a 4D decoupled Hofstadter model, where the second Chern number could be factorized as a product of two first Chern numbers. More generally, let us consider the characteristic function

$$\Psi(x) = \text{sign}\{\cos(2\pi\phi_1 x) + \cos[2\pi\phi_2(\epsilon x + y)]\}, \quad (13)$$

with ϵ being either 0 (yielding the decoupled model) or 1 (yielding the coupled model introduced in reference [68], where the factorization of the second Chern number no longer holds). This function is invariant under discrete translations, with crystal vectors $\mathbf{a}_1 = q_1(1, -\epsilon)$ and $\mathbf{a}_2 = q_2(0, 1)$. The reciprocal vectors are therefore $\mathbf{b}_1 = \frac{2\pi}{q_1}(1, 0)$ and $\mathbf{b}_2 = \frac{2\pi}{q_2}(\epsilon, 1)$, so that $\mathbf{a}_i \cdot \mathbf{b}_j = 2\pi\delta_{ij}$. The edges of the RBZ are quasi-momenta of the form

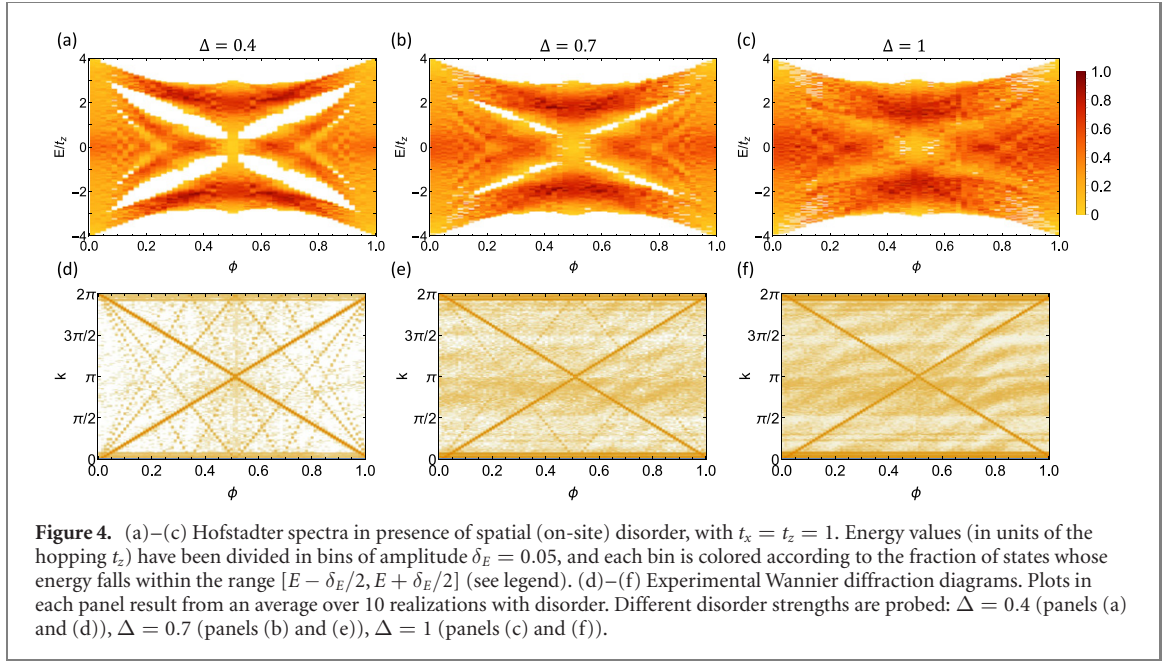
$$\mathbf{k} = r_1\mathbf{b}_1 + r_2\mathbf{b}_2, \quad (14)$$

where $r_1 = p_1\nu_1 + q_1s_1$ and $r_2 = p_2\nu_2 + q_2s_2$. This gives

$$\frac{\mathbf{k}}{2\pi} = \left(\frac{r_1}{q_1} + \epsilon\frac{r_2}{q_2}, \frac{r_2}{q_2}\right). \quad (15)$$

The second Chern number is given by

$$C_2 = \frac{\partial^2 \left(\frac{r_1 r_2}{q_1 q_2}\right)}{\partial \phi_1 \partial \phi_2} = \frac{\partial^2}{\partial \phi_1 \partial \phi_2} \left[\left(\frac{k_x}{2\pi} - \epsilon\frac{k_y}{2\pi}\right) \frac{k_y}{2\pi} \right] = \frac{\partial^2}{\partial \phi_1 \partial \phi_2} \left(\frac{k_x k_y}{(2\pi)^2} - \epsilon \frac{k_y^2}{(2\pi)^2} \right). \quad (16)$$



In this more general framework, it is always possible to relate the second Chern number to the position of the diffraction peaks, even though the second Chern number does not factorize.

5. Robustness against disorder

In presence of structural disorder, topological systems are known to be robust as long as the perturbation is much smaller than the corresponding spectral gap. Here we probe, both numerically and experimentally, the robustness of the Wannier diffraction diagram corresponding to the 2D Hofstadter model.

Figures 4(a)–(c) show the energy spectra of the 2D Hofstadter model, in presence of a disorder potential $V_{\text{dis}} = t_z \xi(x)$, where $\xi(x)$ represents random numbers ranging in $[-\Delta, \Delta]$, Δ denoting the disorder strength. The on-site disorder has been optically implemented by slightly altering the 1D characteristic function:

$$\chi_{\text{dis}}(x) = \text{sign}[\cos(2\pi\phi x) + d + \xi(x)], \quad (17)$$

with $d = 0.25$.

Experimental diagrams obtained for the different disorder strengths are plotted in figures 4(d)–(f). Each plot in figure 4 results from an average over 10 realizations in presence of the picked level of disorder. It is evident that diffraction orders associated with small spectral gaps are rapidly washed away, while the 1st-order Bragg peaks, which are associated with the largest gaps of the spectrum, remain visible even for the largest disorder (i.e. $\Delta = 1$). This proves that the main properties of the Wannier diffraction diagram are robust against disorder, as expected for topological features.

6. Conclusions and outlook

In this paper, we showed that the topological properties of crystal electrons in presence of a constant magnetic field in 2, 3 and 4 spatial dimensions solely depend on the translational symmetry of the effective magnetic lattices. By means of a compact and intuitive genuinely-optical architecture, we succeeded in linking the topological invariants of the Hofstadter Hamiltonians to diffraction figures generated by photonic gratings that reflect the essential symmetries of the original model. Remarkably, such a connection is established within a single experimental realization, in contrast to other methods which typically rely on populating a subset of states. This is especially notable for 3D and 4D, where multiple topological invariants are required for each gap and where complete topological characterizations have not yet been achieved in experiments. In the future, it will be interesting to further generalize our method to probe even higher-dimensional extensions or other classes of topological models. In 4D, for example, a non-zero second Chern number may arise in systems featuring time-reversal symmetry, e.g. with spin-dependent

gauge fields, in which all first Chern numbers vanish [20, 21, 23, 26]. In our implementation, the role of spin may be played by the polarization degree of freedom of the light beam.

Acknowledgments

We wish to thank E Prodan for very insightful discussions. FDC, ADE, LM and FC acknowledge support from the EU (Horizon 2020 program, under ERC PHOSPhOR 694683). MM acknowledges support from the Foundational Questions Institute Fund (Grant No. FQXi-IAF19-05), and from the ANR Research Collaborative Project ‘Qu-DICE’ (ANR-PRC-CES47). HMP is supported by the Royal Society via Grants UF160112, RGF\EA\180121 and RGF\R1\180071. AD and ML acknowledge support from: ERC AdG NOQIA; Agencia Estatal de Investigación (R & D project CEX2019-000910-S, funded by MCIN/AEI/10.13039/501100011033, Plan National FIDEUA PID2019-106901GB-I00, FPI, QUANTERA MAQS PCI2019-111828-2, Proyectos de I+D+I ‘Retos Colaboración’ RTC2019-007196-7); Fundació Cellex; Fundació Mir-Puig; Generalitat de Catalunya through the CERCA program, AGAUR Grant No. 2017 SGR 134, QuantumCAT U16-011424, co-funded by ERDF Operational Program of Catalonia 2014-2020; EU Horizon 2020 FET-OPEN OPTOLogic (Grant No. 899794); National Science Centre, Poland (Symfonia Grant No. 2016/20/W/ST4/00314); Marie Skłodowska-Curie grant STREDCH No 101029393; ‘La Caixa’ Junior Leaders fellowships (ID100010434) and EU Horizon 2020 under Marie Skłodowska-Curie Grant Agreement No. 847648 (LCF/BQ/PI19/11690013, LCF/BQ/PI20/11760031, LCF/BQ/PR20/11770012, LCF/BQ/PR21/11840013). PM was supported by Grant PID2020-113565GB-C21 funded by MCIN/AEI/10.13039/501100011033, and EU FEDER Quantumcat. This research was supported in part by the National Science Foundation under Grant No. NSF PHY-1748958.

Data availability statement

The data that support the findings of this study are available upon reasonable request from the authors.

Appendix A. Details of the experimental setup

The experiment has been realized by studying the far-field diffraction patterns of a He–Ne laser beam (operating wavelength: $\lambda = 632.8$ nm) impinging on a spatial light modulator (SLM). The SLM is a liquid-crystal (LC) device where the extraordinary refractive index has an inhomogeneous distribution that can be controlled and dynamically changed with a computer. This is achieved by means of an array of 1920×1152 pixels (of side $9.2 \mu\text{m}$), each one consisting of an electrode whose voltage independently tunes the local out-of-plane orientation of the LCs below it. This allows to manipulate the spatial phase distribution of the impinging beam, e.g. to display the desired transmission functions, as long as the beam is polarized along the extra-ordinary axis of the LCs.

Assuming a plane-wave incident wave-front, when imaging the diffracted light on the focal plane of a converging lens, one accesses the Fourier transform of the chosen transmission function. For instance, the transmission function $\chi(x) = \text{sign}[\cos(2\pi p/qx) + d]$ was implemented by displaying the phase pattern $g(x) = \pi(3 + \chi(x))/2$. Since the input beam polarization can be not perfectly aligned with the extraordinary axis of the liquid crystals, we added to $g(x)$ the blazing function $2\pi y/\Lambda \bmod 2\pi$, with Λ chosen to be small enough to spatially separate the light diffracted by the SLM from the 0th (unmodulated) diffraction order in the Fourier plane (in our experiment, a convenient choice was $\Lambda = 150$ pixels).

We displayed the pattern associated with $\chi(x)$ choosing $q = 353$ and varying p from 0 to q . The corresponding lattice step size was chosen equal to $n_x = 4$ pixels, thus building a grating consisting of 480 sites. The Fourier-transforming lens had focal length $f = 30$ cm. These parameters were chosen to avoid overlap of diffracted light spots, and to image all the Brillouin zone on the camera sensor. In the experiment, the effective lattice length L , to be considered for simulating numerically the diffraction pattern, was determined by the transverse width of the beam. Assuming an input Gaussian beam of transverse intensity proportional to $\exp(-2r^2/w^2)$, we measured a beam waist $w = 1.72 \pm 0.05$ mm. This implies that we were illuminating a portion of the SLM corresponding to ≈ 100 lattice sites. Numerical simulations of the diffraction of a plane-wave impinging on a finite lattice of $L = 100$ sites reproduces with good approximation the intensity patterns detected experimentally (see next section).

Appendix B. Analytic expression of the diffraction figure for the 2D Hofstadter experiment

Let us consider a grating S_L made up of L sites, whose periodicity is modulated by the square pulse $\chi(x)$ defined in equation (4), and let us define $d \equiv \sin(\delta/2)$. The diffracted field results

$$f(k) = \frac{1}{\sqrt{L}} \sum_{x=0}^{L-1} \chi(x) e^{ikx} = \frac{1}{\sqrt{L}} \sum_{x=0}^{L-1} \text{sign} \left[\cos \left(\frac{2\pi x p}{q} \right) + \sin(\delta/2) \right] e^{ikx}, \quad (\text{B1})$$

where we restrict the choice of δ to the range $[0, \pi]$. Since the system is finite, k takes discrete values: $k \equiv 2\pi l/L$, with $l \in [-L/2, L/2]$.

In order to explicitly evaluate equation (B1), we replace $\chi(x)$ with its Fourier series. The real (A_n) and the imaginary (B_n) part of the Fourier coefficients are given by

$$\begin{aligned} A_n &\equiv \frac{1}{T} \int_0^T dx \chi(x) \cos(n\Omega x), \\ B_n &\equiv \frac{1}{T} \int_0^T dx \chi(x) \sin(n\Omega x), \end{aligned} \quad (\text{B2})$$

where $\Omega \equiv 2\pi/T = 2\pi p/q = 2\pi\phi$ is the frequency of the square pulse (i.e. $1/\phi$ is its spatial period) and $n \in \mathbb{N}$. Performing these integrals we obtain:

$$A_0 = \frac{\delta}{\pi}, \quad A_n = \frac{2(-1)^{n+1} \sin \left[n \frac{(\pi-\delta)}{2} \right]}{\pi n}, \quad B_n = 0. \quad (\text{B3})$$

The constant δ controls the number of visible lines in the Wannier diffraction diagram. In order to resolve a large number of peaks, we choose δ so that the visibility of the 6th diffraction peak is maximized. Since the first maximum of $A_6(\delta)$ occurs at $\delta \sim 0.5$, we pick $d = \sin(\delta/2) \sim 0.25$. The Fourier expansion of $\chi(x)$ reads

$$\chi(x) = \sum_{n=0}^{\infty} A_n \cos(2\pi\phi n x) = \sum_{n=1}^q \tilde{A}_n \cos(2\pi\phi n x), \quad (\text{B4})$$

where $\tilde{A}_n = \sum_{s=0}^{\infty} A_{n+sq}$. To reach the last equality, we used the periodicity of the function to fold the Fourier spectrum over a range of q harmonics. It becomes clear now that each harmonic component of the pulse corresponds to one eigenvalue of the Harper equation (1) in the limit of vanishing $t_x \ll t_z$, multiplied by a coefficient \tilde{A}_n which modulates relative intensities. We stress here that the previous limit is properly addressed in the context of adiabatic perturbation theory, as rigorously discussed in reference [4]. Under those conditions, the gaps open at momenta k_x given by a Diophantine equation *identical* to the one determining the conductivity. Inserting equation (B4) in equation (B1), we find

$$f(k) = \sum_{x=0}^{L-1} \sum_{n=1}^q \frac{\tilde{A}_n}{2\sqrt{L}} (e^{i[k-n\Omega]x} + e^{i[k+n\Omega]x}). \quad (\text{B5})$$

The two summations can be swapped (since they both converge to finite quantities), so we can first evaluate the one over x :

$$\zeta_{\pm} \equiv \sum_{x=0}^{L-1} e^{i(k \pm n\Omega)x} = \frac{1 - e^{\pm i 2\pi\phi L}}{1 - e^{i 2\pi \left(\frac{l}{L} \pm n\phi \right)}}, \quad (\text{B6})$$

where we used $k = 2\pi l/L$. Therefore, the explicit expression of the Fourier expansion of the field reads

$$f(l) = f_0(l) + \sum_{n=1}^{\infty} \frac{2(-1)^{n+1} \sin \left[n \frac{(\pi-\delta)}{2} \right]}{2\pi n \sqrt{L}} (\zeta_+ + \zeta_-) = f_0(l) + \sum_{n=1}^{q-1} \frac{\tilde{A}_n}{2\sqrt{L}} (\zeta_+ + \zeta_-), \quad (\text{B7})$$

where $f_0(l) \equiv \frac{2\delta}{\pi} \frac{1-i \sin(2\pi\phi L)}{1-e^{i 2\pi l/L}}$.

For $L \rightarrow \infty$, each term in equation (B7) is a sum of two Dirac delta-like contributions: $\zeta_{\pm} \propto \delta \left(\frac{l}{L} \pm n\phi \right)$, with $\phi = p/q$. For finite L , there are two possible scenarios: L may or may not be a multiple of q . When L is a multiple of q , namely $L = zq$ (with integer z), we find the same result as in the infinite case and $f_n(l) \neq 0$ only when $l/L = \pm np/q$, that is $l = \pm znp$. Since the main contribution to the diffracted field comes from the first harmonic $n = 1$, the brightest peaks appear at $l = \pm zp$. When L is not a multiple of q , we find non-zero diffracted field for many more values of l , which contribute to creating the fractal spectrum typical of quasi-crystals. Nevertheless, the brightest peaks still appear at $l = \pm zp$, with $z = \text{Floor}[L/q]$.

Appendix C. Diophantine equation in 2D

Here we demonstrate how the 2D Diophantine equation may be derived from the magnetic translational symmetry of the lattice Hamiltonian [63, 69]. Let us consider spinless fermions on a square lattice under the action of a constant magnetic field with a magnetic flux $\phi = p/q$ per plaquette. In the Landau gauge, the Hamiltonian reads

$$H = \sum_{m,n} -t_x c_{m+1,n}^\dagger c_{m,n} - t_z e^{-2\pi i \phi m} c_{m,n+1}^\dagger c_{m,n} + \text{h.c.} \quad (\text{C1})$$

In presence of a non-zero magnetic flux, this Hamiltonian is no longer commuting with the lattice translation operator T_z . This motivates the introduction of the ‘magnetic translation operators’

$$\begin{aligned} M_x &= \sum_{m,n} c_{m+1,n}^\dagger c_{m,n}, \\ M_z &= \sum_{m,n} e^{-2\pi i \phi m} c_{m,n+1}^\dagger c_{m,n}. \end{aligned} \quad (\text{C2})$$

These operators commute with the Hamiltonian, but not with each other: $M_x M_z = e^{-2\pi i \phi} M_z M_x$. However, $(M_x)^q$ commutes with M_z , so that $\{H, (M_x)^q, M_z\}$ form a ‘complete set of commuting operators’. Therefore, one has to consider a magnetic unit cell of at least q sites in the x -direction in order to apply the Bloch theorem. Let us first focus on the ground band, which we assume to be non-degenerate. The eigenstates of the Hamiltonian within this band are Bloch states of the form [70]

$$\psi_{\mathbf{k}}(m, n) = e^{-i(k_x m + k_z n)} e^{2\pi i \phi m n} u_{\mathbf{k}}(m), \quad (\text{C3})$$

where k_x and k_z are varying in an RBZ, defined by $0 < k_x \leq 2\pi/q$ and $0 < k_z \leq 2\pi$, $u_{k_x, k_z}(m+q) = u_{k_x, k_z}(m)$ and we omit the band index and take the lattice spacings equal to one for simplicity. Since M_x and M_z commute with the Hamiltonian, $\psi_{\mathbf{k}}$ can be simultaneous eigenvectors of both M_x and M_z (i.e., $\psi_{\mathbf{k}}, M_x \psi_{\mathbf{k}}$, and $M_z \psi_{\mathbf{k}}$ all have the same energy $\epsilon_{\mathbf{k}}$, and represent the same state, up to a phase factor). Such Bloch states satisfy the relations

$$\begin{aligned} (M_x)^q \psi_{\mathbf{k}}(m, n) &= \psi_{\mathbf{k}}(m+q, n) = e^{ik_x q} \psi_{\mathbf{k}}(m, n), \\ M_z \psi_{\mathbf{k}}(m, n) &= e^{-2\pi i \phi m} \psi_{\mathbf{k}}(m, n+1) = e^{ik_z} \psi_{\mathbf{k}}(m, n), \end{aligned} \quad (\text{C4})$$

as required for the Bloch theorem.

This expression has still some residual degrees of freedom originating from the momentum-space periodicity of $u_{\mathbf{k}}$. Indeed, M_x is a standard translation operator, so that $u_{k_x+2\pi/q, k_z} = u_{k_x, k_z}$ (omitting the spatial indices). Along the other direction, instead, M_z is not a standard translation operator, so that Bloch theorem does not apply and there is some extra freedom: $u_{k_x, k_z+2\pi} = e^{i\zeta(\mathbf{k})} u_{k_x, k_z}$. This implies

$$e^{i\zeta(\mathbf{k})} u_{\mathbf{k}} = u_{k_x, k_z+2\pi} = u_{k_x+2\pi/q, k_z+2\pi} = e^{i\zeta(k_x+2\pi/q, k_z)} u_{\mathbf{k}}, \quad (\text{C5})$$

so that $\zeta(k_x+2\pi/q, k_z) = \zeta(\mathbf{k}) + 2\pi C_1$, with C_1 an integer number. The simplest function satisfying this condition is $\zeta(\mathbf{k}) = k_x q C_1$, and $2\pi C_1$ is the phase acquired as the wavefunction is parallelly-transported around the whole RBZ, and therefore C_1 may be readily identified as the Chern number of the ground band.

There is yet an additional gauge freedom arising from the non-commutativity of the magnetic translation operators. Since

$$M_z M_x \psi_{\mathbf{k}} = e^{2\pi i \phi} M_x M_z \psi_{\mathbf{k}} = e^{i(k_z+2\pi\phi)} M_x \psi_{\mathbf{k}} \quad (\text{C6})$$

and $M_z \psi_{k_x, k_z+2\pi\phi} = e^{i(k_z+2\pi\phi)} \psi_{k_x, k_z+2\pi\phi}$, we find that $M_x \psi_{\mathbf{k}}$ and $\psi_{k_x, k_z+2\pi\phi}$ must represent the same state, up to a phase factor:

$$M_x \psi_{\mathbf{k}} = e^{i\eta(\mathbf{k})} \psi_{k_x, k_z+2\pi\phi}. \quad (\text{C7})$$

This leads to

$$\begin{aligned} e^{i\eta(\mathbf{k})} \psi_{k_x, k_z+2\pi\phi} &= M_x \psi_{\mathbf{k}} = M_x \psi_{k_x+2\pi/q, k_z} = e^{i\eta(k_x+2\pi/q, k_z)} \psi_{k_x+2\pi/q, k_z+2\pi\phi} \\ &= e^{i\eta(k_x+2\pi/q, k_z)} \psi_{k_x, k_z+2\pi\phi}. \end{aligned} \quad (\text{C8})$$

Proceeding as above, one finds that the simplest functional form for the phase factor is $\eta(\mathbf{k}) = k_x q S_1$, with S_1 an integer number.

To derive the Diophantine equation, let us now consider a translation by a whole magnetic cell (along its extended direction), which gives

$$\begin{aligned}(M_x)^q \psi_{\mathbf{k}} &= e^{ik_x q^2 S_1} \psi_{k_x, k_z + 2\pi p} = e^{ik_x q(qS_1 + pC_1)} \psi_{k_x, k_z} \\ &= e^{ik_x q} \psi_{k_x, k_z},\end{aligned}\quad (C9)$$

where in the last step we have used the fact that the translation by a whole magnetic cell generated by $(M_x)^q$ results in a simple phase factor $e^{ik_x q}$. This finally leads to the Diophantine equation for the ground band:

$$pC_1 + qS_1 = 1. \quad (C10)$$

This equation has a unique solution provided that p and q are coprime and $|C_1| < q/2$. Considering now multiple bands, the same treatment as above may be performed for each band, obtaining $pC_i + qS_i = 1$. Let us now recall that the i th Chern number is linked to the Hall conductivities of the neighboring gaps by $C_i = \nu_i - \nu_{i-1}$, and let us assume similarly that $S_i = s_i - s_{i-1}$, with $\nu_0 = s_0 = 0$. Summing the equations over all the gaps, one readily obtains the usual Diophantine equation

$$p\nu_r + qs_r = r, \quad (C11)$$

where $\nu_r = \sum_{i=1}^r C_i$ is the Hall conductivity. Again, the solution is unique provided that $|\nu_r| < q/2$.

Appendix D. Diophantine equation in 3D

By closely following the steps of the previous section, here we derive the 3D Diophantine equation equation (7) from the magnetic translation symmetry of the 3D Hofstadter model [69].

First, we set the following periodic boundary conditions on the Bloch functions:

$$\begin{aligned}u_{k_x + 2\pi/Q, k_y, k_z} &= u_{\mathbf{k}}, \\ u_{k_x, k_y + 2\pi, k_z} &= e^{ik_x \sigma_y Q} u_{\mathbf{k}}, \\ u_{k_x, k_y, k_z + 2\pi} &= e^{ik_x \sigma_z Q} u_{\mathbf{k}},\end{aligned}\quad (D1)$$

where we refer to the band Chern numbers as σ_α , and we omit the band index and set the lattice spacings equal to one again.

Applying the 3D magnetic translation operator M_x to $u_{\mathbf{k}}$, we obtain

$$M_x u_{\mathbf{k}} = e^{i k_x Q} u_{k_x, k_y + 2\pi \phi_y, k_z + 2\pi \phi_z}. \quad (D2)$$

By reiterating this application Q times and invoking the boundary conditions (D1), one is led to

$$e^{i k_x Q} u_{\mathbf{k}} = e^{i k_x Q(\sigma_y m_y P + \sigma_z m_z P + SQ)} u_{\mathbf{k}}, \quad (D3)$$

where we set $\phi_y = m_y P/Q$ and $\phi_z = m_z P/Q$. Equation (D3) is satisfied if

$$\sigma_y m_y P + \sigma_z m_z P + SQ = 1. \quad (D4)$$

The 3D Diophantine equation

$$\nu_y^{(r)} m_y P + \nu_z^{(r)} m_z P + s^{(r)} Q = r \quad (D5)$$

is obtained from equation (D4), by recalling $\sigma_\alpha^{(r)} = \nu_\alpha^{(r)} - \nu_\alpha^{(r-1)}$.

ORCID iDs

Francesco Di Colandrea  <https://orcid.org/0000-0002-4863-1448>

Alessio D'Errico  <https://orcid.org/0000-0002-6964-4328>

Hannah M Price  <https://orcid.org/0000-0002-1377-596X>

Maciej Lewenstein  <https://orcid.org/0000-0002-0210-7800>

Lorenzo Marrucci  <https://orcid.org/0000-0002-1154-8966>

Filippo Cardano  <https://orcid.org/0000-0002-7828-3819>

Alexandre Dauphin  <https://orcid.org/0000-0003-4996-2561>

Pietro Massinan  <https://orcid.org/0000-0003-1545-792X>

References

- [1] von Klitzing K 1986 The quantized Hall effect *Rev. Mod. Phys.* **58** 519
- [2] Hofstadter D R 1976 Energy levels and wave functions of Bloch electrons in rational and irrational magnetic fields *Phys. Rev. B* **14** 2239
- [3] Thouless D J, Kohmoto M, Nightingale M P and den Nijs M 1982 Quantized Hall conductance in a two-dimensional periodic potential *Phys. Rev. Lett.* **49** 405
- [4] Kohmoto M 1989 Zero modes and the quantized Hall conductance of the two-dimensional lattice in a magnetic field *Phys. Rev. B* **39** 11943
- [5] Niu Q, Thouless D J and Wu Y-S 1985 Quantized Hall conductance as a topological invariant *Phys. Rev. B* **31** 3372
- [6] Avron J E, Seiler R and Simon B 1983 Homotopy and quantization in condensed matter physics *Phys. Rev. Lett.* **51** 51
- [7] Halperin B I 1987 Possible states for a three-dimensional electron gas in a strong magnetic field *Japan. J. Appl. Phys.* **26** 1913
- [8] Montambaux G and Kohmoto M 1990 Quantized Hall effect in three dimensions *Phys. Rev. B* **41** 11417
- [9] Kohmoto M, Halperin B I and Wu Y-S 1992 Diophantine equation for the three-dimensional quantum Hall effect *Phys. Rev. B* **45** 13488
- [10] Haavasoja T, Störmer H L, Bishop D J, Narayanamurti V, Gossard A C and Wiegmann W 1984 Magnetization measurements on a two-dimensional electron system *Surf. Sci.* **142** 294
- [11] Störmer H L, Eisenstein J P, Gossard A C, Wiegmann W and Baldwin K 1986 Quantization of the Hall effect in an anisotropic three-dimensional electronic system *Phys. Rev. Lett.* **56** 85
- [12] Druist D P, Turley P J, Maranowski K D, Gwinn E G and Gossard A C 1998 Observation of chiral surface states in the integer quantum Hall effect *Phys. Rev. Lett.* **80** 365
- [13] Koshino M, Aoki H, Kuroki K, Kagoshima S and Osada T 2001 Hofstadter butterfly and integer quantum Hall effect in three dimensions *Phys. Rev. Lett.* **86** 1062
- [14] Koshino M and Aoki H 2003 Integer quantum Hall effect in isotropic three-dimensional crystals *Phys. Rev. B* **67** 195336
- [15] Brüning J, Demidov V V and Geyler V A 2004 Hofstadter-type spectral diagrams for the Bloch electron in three dimensions *Phys. Rev. B* **69** 033202
- [16] Roy S, Kolodrubetz M, Moore J E and Grushin A G 2016 Chern numbers and chiral anomalies in Weyl butterflies *Phys. Rev. B* **94** 161107
- [17] Lu L, Gao H and Wang Z 2018 Topological one-way fiber of second Chern number *Nat. Commun.* **9** 5384
- [18] Avron J E, Sadun L, Segert J and Simon B 1988 Topological invariants in Fermi systems with time-reversal invariance *Phys. Rev. Lett.* **61** 1329
- [19] Fröhlich J and Pedrini B 2000 New applications of the chiral anomaly *Mathematical Physics 2000* (London, United Kingdom: Imperial College Press) pp 9–47
- [20] Zhang S-C and Hu J 2001 A four-dimensional generalization of the quantum Hall effect *Science* **294** 823
- [21] Qi X-L, Hughes T L and Zhang S-C 2008 Topological field theory of time-reversal invariant insulators *Phys. Rev. B* **78** 195424
- [22] Edge J M, Tworzydło J and Beenakker C W J 2012 Metallic phase of the quantum Hall effect in four-dimensional space *Phys. Rev. Lett.* **109** 135701
- [23] Kraus Y E, Ringel Z and Zilberberg O 2013 Four-dimensional quantum Hall effect in a two-dimensional quasicrystal *Phys. Rev. Lett.* **111** 226401
- [24] Price H M, Zilberberg O, Ozawa T, Carusotto I and Goldman N 2015 Four-dimensional quantum Hall effect with ultracold atoms *Phys. Rev. Lett.* **115** 195303
- [25] Price H M, Zilberberg O, Ozawa T, Carusotto I and Goldman N 2016 Measurement of Chern numbers through center-of-mass responses *Phys. Rev. B* **93** 245113
- [26] Price H M 2020 Four-dimensional topological lattices through connectivity *Phys. Rev. B* **101** 205141
- [27] Lohse M, Schweizer C, Price H M, Zilberberg O and Bloch I 2018 Exploring 4D quantum Hall physics with a 2D topological charge pump *Nature* **553** 55
- [28] Zilberberg O, Huang S, Guglielmon J, Wang M, Chen K P, Kraus Y E and Rechtsman M C 2018 Photonic topological boundary pumping as a probe of 4D quantum Hall physics *Nature* **553** 59
- [29] Sugawa S, Salces-Carcoba F, Perry A R, Yue Y and Spielman I B 2018 Second Chern number of a quantum-simulated non-abelian Yang monopole *Science* **360** 1429
- [30] Wang Y, Price H M, Zhang B and Chong Y D 2020 Circuit implementation of a four-dimensional topological insulator *Nat. Commun.* **11** 2356
- [31] Chen Z-G, Zhu W, Tan Y, Wang L and Ma G 2021 Acoustic realization of a four-dimensional higher-order Chern insulator and boundary-modes engineering *Phys. Rev. X* **11** 011016
- [32] Petrides I and Zilberberg O 2020 Higher-order topological insulators, topological pumps and the quantum Hall effect in high dimensions *Phys. Rev. Res.* **2** 022049
- [33] Goldman N, Juzeliūnas G, Öhberg P and Spielman I B 2014 Light-induced gauge fields for ultracold atoms *Rep. Prog. Phys.* **77** 126401
- [34] Ozawa T *et al* 2019 Topological photonics *Rev. Mod. Phys.* **91** 015006
- [35] Cooper N R, Dalibard J and Spielman I B 2019 Topological bands for ultracold atoms *Rev. Mod. Phys.* **91** 015005
- [36] Aidelsburger M, Lohse M, Schweizer C, Atala M, Barreiro J T, Nascimbène S, Cooper N R, Bloch I and Goldman N 2014 Measuring the Chern number of Hofstadter bands with ultracold bosonic atoms *Nat. Phys.* **11** 162
- [37] Asteria L, Tran D T, Ozawa T, Tarnowski M, Rem B S, Fläschner N, Sengstock K, Goldman N and Weitenberg C 2019 Measuring quantized circular dichroism in ultracold topological matter *Nat. Phys.* **15** 449
- [38] Kraus Y E, Lahini Y, Ringel Z, Verbin M and Zilberberg O 2012 Topological states and adiabatic pumping in quasicrystals *Phys. Rev. Lett.* **109** 106402
- [39] Mittal S, Orre V V, Leykam D, Chong Y D and Hafezi M 2019 Photonic anomalous quantum Hall effect *Phys. Rev. Lett.* **123** 043201
- [40] D'Errico A *et al* 2020 Two-dimensional topological quantum walks in the momentum space of structured light *Optica* **7** 108
- [41] Ni X, Chen K, Weiner M, Apigo D J, Prodan C, Alù A, Prodan E and Khanikaev A B 2019 Observation of Hofstadter butterfly and topological edge states in reconfigurable quasi-periodic acoustic crystals *Commun. Phys.* **2** 55

- [42] Tang F *et al* 2019 Three-dimensional quantum Hall effect and metal-insulator transition in ZrTe₅ *Nature* **569** 537
- [43] Krinner S, Stadler D, Husmann D, Brantut J-P and Esslinger T 2014 Observation of quantized conductance in neutral matter *Nature* **517** 64
- [44] Umucalilar R O, Zhai H and Oktel M O 2008 Trapped Fermi gases in rotating optical lattices: realization and detection of the topological Hofstadter insulator *Phys. Rev. Lett.* **100** 070402
- [45] Bardyn C-E, Huber S D and Zilberberg O 2014 Measuring topological invariants in small photonic lattices *New J. Phys.* **16** 123013
- [46] Tran D T, Dauphin A, Grushin A G, Zoller P and Goldman N 2017 Probing topology by ‘heating’: quantized circular dichroism in ultracold atoms *Sci. Adv.* **3** e1701207
- [47] Wang C, Zhang P, Chen X, Yu J and Zhai H 2017 Scheme to measure the topological number of a Chern insulator from quench dynamics *Phys. Rev. Lett.* **118** 185701
- [48] Cardano F *et al* 2017 Detection of Zak phases and topological invariants in a chiral quantum walk of twisted photons *Nat. Commun.* **8** 15516
- [49] Tarnowski M, Ünal F N, Fläschner N, Rem B S, Eckardt A, Sengstock K and Weitenberg C 2019 Measuring topology from dynamics by obtaining the Chern number from a linking number *Nat. Commun.* **10** 1728
- [50] Wannier G H 1978 A result not dependent on rationality for Bloch electrons in a magnetic field *Phys. Status Solidi b* **88** 757
- [51] Price H M and Cooper N R 2012 Mapping the Berry curvature from semiclassical dynamics in optical lattices *Phys. Rev. A* **85** 033620
- [52] Dauphin A and Goldman N 2013 Extracting the Chern number from the dynamics of a Fermi gas: implementing a quantum Hall bar for cold atoms *Phys. Rev. Lett.* **111** 135302
- [53] Thouless D J 1983 Quantization of particle transport *Phys. Rev. B* **27** 6083
- [54] Lohse M, Schweizer C, Zilberberg O, Aidelsburger M and Bloch I 2015 A Thouless quantum pump with ultracold bosonic atoms in an optical superlattice *Nat. Phys.* **12** 350
- [55] Nakajima S, Tomita T, Taie S, Ichinose T, Ozawa H, Wang L, Troyer M and Takahashi Y 2016 Topological Thouless pumping of ultracold fermions *Nat. Phys.* **12** 296
- [56] Shechtman D, Blech I, Gratias D and Cahn J W 1984 Metallic phase with long-range orientational order and no translational symmetry *Phys. Rev. Lett.* **53** 1951
- [57] Prodan E 2015 Virtual topological insulators with real quantized physics *Phys. Rev. B* **91** 245104
- [58] Dareau A, Levy E, Aguilera M B, Bouganne R, Akkermans E, Gerbier F and Beugnon J 2017 Revealing the topology of quasicrystals with a diffraction experiment *Phys. Rev. Lett.* **119** 215304
- [59] Tanese D *et al* 2014 Fractal energy spectrum of a polariton gas in a Fibonacci quasiperiodic potential *Phys. Rev. Lett.* **112** 146404
- [60] Zilberberg O 2021 Topology in quasicrystals *Opt. Mater. Express* **11** 1143
- [61] Streda P 1982 Theory of quantised Hall conductivity in two dimensions *J. Phys. C: Solid State Phys.* **15** L717
- [62] Streda P 1982 Quantised Hall effect in a two-dimensional periodic potential *J. Phys. C: Solid State Phys.* **15** L1299
- [63] Dana I, Avron Y and Zak J 1985 Quantised Hall conductance in a perfect crystal *J. Phys. C: Solid State Phys.* **18** L679
- [64] Harper P G 1955 Single band motion of conduction electrons in a uniform magnetic field *Proc. Phys. Soc. A* **68** 874
- [65] Repellin C, Léonard J and Goldman N 2020 Fractional Chern insulators of few bosons in a box: Hall plateaus from center-of-mass drifts and density profiles *Phys. Rev. A* **102** 063316
- [66] Janecek S, Aichinger M and Hernández E R 2013 Two-dimensional Bloch electrons in perpendicular magnetic fields: an exact calculation of the Hofstadter butterfly spectrum *Phys. Rev. B* **87** 235429
- [67] Laughlin R B 1981 Quantized Hall conductivity in two dimensions *Phys. Rev. B* **23** 5632
- [68] Mochol-Grzelak M, Dauphin A, Celi A and Lewenstein M 2018 Efficient algorithm to compute the second Chern number in four dimensional systems *Quantum Sci. Technol.* **4** 014009
- [69] de Blas A-Z E and Axel F 2004 Diophantine equation for the 3D transport coefficients of Bloch electrons in a strong tilted magnetic field with quantum Hall effect *J. Phys.: Condens. Matter.* **16** 7673
- [70] Aidelsburger M 2015 *Artificial Gauge Fields with Ultracold Atoms in Optical Lattices* (Berlin: Springer)